ADVANCED MATERIALS INTERFACES
Open Access
www.advmatinterfaces.de

FIB-SEM and ToF-SIMS Analysis of High-Temperature PEM Fuel Cell Electrodes

*Michael Braig, Niklas H. Deissler, Ildiko Lüdeking, Fabian Regnet, Nico Bevilacqua, and Roswitha Zeis**

The phosphoric acid (PA) distribution in the electrodes is a crucial factor for the performance of high-temperature polymer electrolyte fuel cells (HT-PEM FCs). Therefore, understanding and optimizing the electrolyte distribution is vital to maximizing power output and achieving low degradation. Although challenging, tracking the PA in nanometer-sized pores is essential because most active sites in the commonly used carbon black-supported catalysts are located in pores below 1 µm. For this study, a cell is operated at 200 mA cm^{-2} for 5 days. After this break-in period, the cathode is separated from the membrane electrode assembly and subsequently investigated by cryogenic focused ion beam scanning electron microscopy (cryo FIB-SEM) coupled with energy-dispersive X-ray spectroscopy (EDX) and time-of-flight secondary ion mass spectrometry (ToF-SIMS). PA is located on the surface and in the bulk of the cathode catalyst layer. In addition, the PA distribution can be successfully linked to the gas diffusion electrode morphology and the binder distribution. The PA preferably invades nanometer-sized pores and is uniformly distributed in the catalyst layer.

1. Introduction

High-temperature polymer electrolyte fuel cells (HT-PEM FCs) contain a phosphoric acid (PA) doped polybenzimidazole (PBI) membrane, which is sandwiched between two gas diffusion electrodes (GDEs). Before cell assembly, the membrane is doped with PA. During cell activation, PA percolates from the membrane into the GDEs; thus, significantly enlarging the triple-phase boundary. While a high electrolyte content in the GDEs improves ionic conductivity, it inhibits reactant diffusion. The oxygen reduction reaction (ORR) on the cathode is particularly affected because oxygen diffusion is sluggish in phosphoric acid, and phosphate anion adsorption on the platinum catalyst blocks active sites.[1,2] Ideally, the PA should be distributed uniformly in the GDE as a thin film over the entire electrode surface to achieve a high triple-phase boundary, high ion conductivity, and low mass transport resistance. Understanding and optimizing the PA distribution is crucial for improving cell performance and reducing degradation.

Generally, GDEs contain a binder to improve the electrodes' mechanical stability and control the PA migration and distribution. Different binders have been evaluated in the literature,[3–5] and new binders are currently being investigated.[6] However, polytetrafluoroethylene (PTFE) is still widely used due to its high chemical stability in the acidic environment at elevated temperatures, good mechanical properties, and hydrophobicity, thereby regulating the acid uptake of the GDE.[7–10] The PTFE particles ideally should be distributed uniformly in the catalyst layer (CL) to achieve a homogenous PA distribution and maximize the electrode stability. Large agglomerations may block pores and decrease the catalytically active surface area because PTFE is an insulator. Thus, a homogenous electrode and an optimized binder content are vital for a homogenous PA distribution.[8,10–12]

PA migration in the membrane and the GDEs was previously visualized by operando synchrotron X-ray tomography experiments.[13–15] The CL pore structure was identified to influence the PA distribution significantly. However, the resolution of X-ray imaging is limited to ≈1 µm,[16] which is insufficient for monitoring the PA in the nanometer-sized pores of the CL. Nonetheless, investigating the PA in this order of magnitude is crucial because most of the CL surface area is found in pores below 1 µm in diameter.[17] The significant impact of the catalyst nanostructure on the PA distribution in HT-PEM FCs was shown by electrochemical impedance spectroscopy (EIS) combined with the distribution of relaxation times (DRT) analysis.[18] Furthermore, ex situ nuclear magnetic resonance (NMR) experiments showed that PA preferably wets micropores in carbon by PA before invading larger mesopores.[19]

M. Braig, N. H. Deissler, N. Bevilacqua, R. Zeis
Karlsruhe Institute of Technology
Helmholtz Institute Ulm
Helmholtzstraße 11, 89081 Ulm, Germany
E-mail: roswitha.zeis@kit.edu
I. Lüdeking, F. Regnet
Center for Solar Energy and Hydrogen Research Baden-Württemberg
Helmholtzstraße 8, 89081 Ulm, Germany
R. Zeis
Department of Mechanical and Industrial Engineering
University of Toronto
5 King's College Road, Toronto ON M5S 3G8, Canada

The ORCID identification number(s) for the author(s) of this article can be found under https://doi.org/10.1002/admi.202202430.

DOI: 10.1002/admi.202202430

Focused ion beam scanning electron microscopy (FIB-SEM) coupled with time of flight secondary ion mass spectrometry (ToF-SIMS) and energy-dispersive X-ray spectroscopy (EDX) was previously employed to characterize element distributions in fuel cell electrodes.[20–24] Combining these methods offers the possibility of a direct correlation between high-resolution secondary electron images and SIMS maps of the same area. While EDX is non-destructive and provides insight into the elemental distribution of the sample, ToF-SIMS damages the sample by milling the surface. This method allows depth profiling and 3D chemical mapping of a sample with a lateral resolution, which is limited by the spot size of the ion beam.

Herein, we present a method capable of simultaneously linking the distribution of a liquid electrolyte to the electrode pore structure and composition with a resolution of 100 nm. After the break-in period, the element composition in the cathode CL of a HT-PEM FC has been mapped via cryo FIB-SEM and ToF-SIMS. Electrochemical impedance spectroscopy (EIS) was employed to monitor cell performance during operation. After 120 h, the cell was disassembled and cooled down in liquid nitrogen to "freeze" the PA distribution during operation. Subsequently, the cathode was separated from the membrane electrode assembly (MEA) and investigated in the FIB-SEM at –150 °C. All electrode components (carbon, PTFE binder, and PA) were successfully mapped.

2. Experimental Section

2.1. Gas Diffusion Electrode Fabrication

Four different GDEs were fabricated in-house by spray coating a catalyst ink onto a commercial gas diffusion layer (GDL) with a microporous layer (MPL, H2315C2, Freudenberg, Germany) with an airbrush system. GDE 1 to 3 were prepared identically by dispersing Vulcan XC72R carbon (Fuel cell store, USA) in a 1:1 mixture of water and isopropanol. A 60 wt% PTFE in water dispersion (Dyneon, 3 M, USA) was added to obtain a PTFE content of ≈6.5% in the dry CL. The ink was subsequently homogenized with a tip sonicator for 30 s and sprayed onto the MPL. During spraying, the GDL was placed on a heating plate at 80 °C to ensure fast evaporation of the solvents. Afterward, the GDEs were cut into squares with an area of 2.2 × 2.2 cm. For GDE 4, the ink was prepared with 20 wt% platinum nanoparticles on Vulcan XC72R (Alfa Aesar, USA) instead of Vulcan XC72R. The subsequent procedure was identical to the other GDEs. The platinum loading was controlled to 1 mgPt cm^{-2} for GDE 4.

The experimental workflow is schematically presented in **Figure 1** and will be described step by step. The properties, measurement settings, and, where applicable, operation conditions of all GDEs are summarized in **Table 1**.

2.2. Membrane Electrode Assembly Fabrication

GDE 3 and GDE 4 were each implemented in a full cell HT-PEM FC setup as anode and cathode. The employed PBI membranes (Dapozol M40, Danish Power Systems, Denmark) were doped in 85% PA for 62 days at room temperature. The doping level was ≈10 g PA per 1 g PBI. The membrane was sandwiched between two polyether ether ketone (PEEK) gaskets, which defined the active cell area to 4 cm^2. The anode and cathode compression was controlled to ≈25 % with PTFE gaskets. The MEA was placed between two stainless steel bipolar plates with serpentine flow fields, which were compressed with a torque of 2 Nm.

2.3. Fuel Cell Characterization

The cells made from GDE 3 and GDE 4 were operated in a test station. The cell temperature was controlled to 160 °C by a heating pad on the outer side of each flow field. A thermocouple was inserted into each bipolar plate to measure the temperature in its center. The gas flows were set to a stoichiometry of 1.8 for hydrogen on the anode and 2.0 for air on the cathode. The cell prepared with GDE 3 was operated at open circuit conditions without any current flow. The cell made from GDE 4 was operated under a constant current density of 200 mA cm^{-2}, which was only interrupted once per day to record an EIS spectrum. Both cells operated for ≈120 h, a typical break-in period for HT-PEM FCs.[18,25,26] At the end of the break-in period, a voltage of 625 mV at 200 mA cm^{-2} was measured for the cell assembled with GDE 4. A polarization curve of a nearly identical cell as the one made from GDE 4 is presented in Figure S1, Supporting Information. However, no cell polarization curve with GDE 4 was recorded because the significantly increased water production at high current density might lead to a considerable PA redistribution.

EIS measurements were performed with a Zahner Zennium potentiostat at a current density of 200 mA cm^{-2} with an amplitude of 2.5 mA cm^{-2}. The cell was set under load with the potentiostat for at least 2 h before the EIS measurement to achieve equilibrium conditions regarding the PA and temperature distribution. The EIS data were further analyzed with the DRT program DRTtools[27] to assign the semicircles of the impedance spectra to individual cell resistances as proposed in refs. [28,29].

2.4. FIB-SEM Coupled With ToF-SIMS

A FIB-SEM from TESCAN (model: S9000G, Brno, Czech Republic) with a built-in custom ToF-SIMS detector from Tofwerk (Thun, Switzerland) and an EDX detector from Oxford (ULTIM MAX 170) was used. The FIB column produced Ga^+-ions and was operated at 30 kV. After recording SEM images and EDX maps, TOF-SIMS measurements were performed (30 kV, 1 nA) in the negative mode. The secondary ions were extracted with 52 kV for extractor 1 and 700 kV for extractor 2. The generated ions were separated according to their mass-to-charge ratio.

Monte Carlo simulations were performed with the software CASINO (v2.4.8.1) to estimate the depth of origin of the back-scattered electron (BSE) and EDX signals. The accelerating voltage for the simulation was 5 kV, which was identical to the voltage under which all BSE and EDX images were recorded.

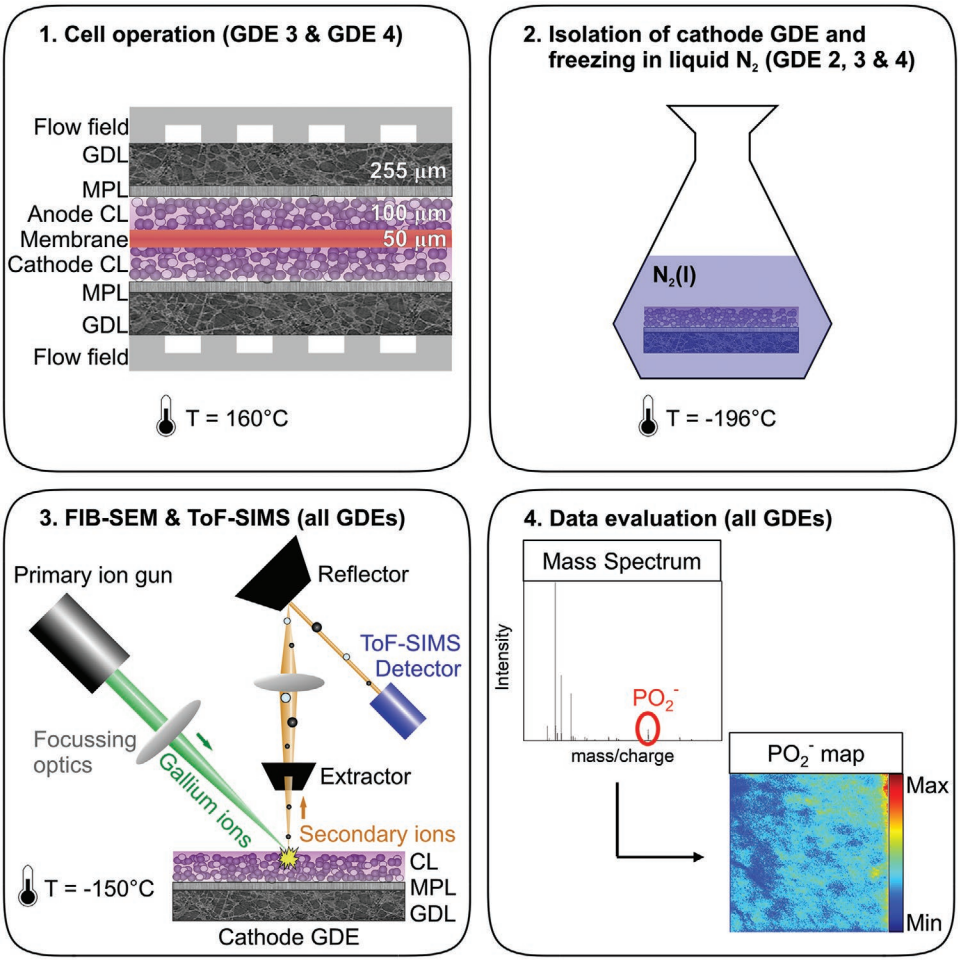

Figure 1. Schematic representation of the experimental workflow. After being operated in a cell setup (step 1, GDE 3, and 4), the cathode GDE is separated from the MEA and subsequently frozen in liquid nitrogen (step 2, GDE 2, 3, and 4). Afterward, SE and BSE images, EDX, and ToF-SIMS maps were recorded in a cryo FIB-SEM at -150 °C (step 3, all GDEs). Last, ions ejected from the sample were identified in the obtained mass spectrum, and a 3D map of every fragment was created (step 4, all GDEs). Here, the PO_2^- signal is shown exemplarily.

For the analyzed material, the properties of phosphoric acid were employed.

GDE 1 was examined in the FIB-SEM at ambient temperature (≈20 °C) without PA doping. GDE 2 was frozen in liquid nitrogen and measured at –150 °C without PA. GDE 3 was doped with PA by implementation into the cell hardware and heated to 160 °C, but no current was applied. GDE 4 was implemented into an operated cell to investigate the acid distribution in the CL under the current flow. After cell operation, the cells made from GDE 3 and 4 were disassembled, and their MEAs were frozen in liquid nitrogen to stabilize the PA distribution. Afterward, the cathode GDEs were separated from the MEA in an EM VCT500 cryo transfer system (Leica, Germany) under a nitrogen atmosphere to prevent the formation of water crystals on the surface. This system ensures the sample transport into the SEM under constant vacuum and cryogenic conditions. Both GDEs were subsequently investigated in the FIB-SEM at –150 °C.

It is believed the PA distribution in the electrode remains nearly constant when the cell pressure is removed. The electrode was transferred as fast as possible into liquid nitrogen to prevent any potential relocation of PA. Furthermore, no PA droplets in GDE were observed, which would indicate a significant redistribution. A redistribution due to the hydrophobic

Table 1. Properties and measurement protocol of the fabricated GDEs.

Sample	Platinum loading [mgPt cm^{-2}]	Phosphoric acid doping of PBI membrane	Cell operation	Freezing in N_2 (l)	SEM temperature [°C]
GDE 1	0	No	–	No	20
GDE 2	0	No	–	Yes	–150
GDE 3	0	Yes	160 °C/0 mA cm^{-2} (5 days)	Yes	–150
GDE 4	1	Yes	160 °C/200 mA cm^{-2} (5 days)	Yes	–150

PTFE binder was also unlikely because PA and carbon were strongly bounded after the operation as FC.

The freezing effect in liquid nitrogen on the GDE structure was examined by comparing results from GDE 1 and 2 because the only difference between both measurements is the freezing process. Comparing the results from GDE 2 and 3 allows for determining the phosphoric acid distribution in the CL under actual membrane doping, compression, and temperature conditions. The only difference between the test routine of GDE 3 and 4 is that GDE 4 was operated as a fuel cell. Thus, the effect of the electrochemically produced water was investigated by comparing GDE 3 and 4.

3. Results and Discussion

3.1. Cathode Catalyst Layer Surface Morphology and Composition

Figure 2 compares the SEM images of the surface of all measured GDEs, which were in contact with the membrane in the assembled cell for GDE 3 and 4. The carbon support is highly electronically conductive and therefore produces sharp images. PA and PTFE; however, cause blurry regions because their conductivity is low.[9,10]

The carbon structure of GDE 1 and GDE 2 looks similar, indicating that the freezing in liquid nitrogen did not impact the electrode structure. Therefore, the freezing process does not alter the results of SEM imaging and can be used without any concerns to conserve the PA distribution in the operated GDEs. The blurry area in the center of GDE 2 can be attributed to PTFE, which typically forms small agglomerations in the CL and is randomly distributed. Low PTFE content leads to smaller agglomerations and more uniform binder distribution, which is beneficial for cell performance and reduces the duration of the break-in period.[9–11] Conversely, GDEs containing a low PTFE content may get flooded with PA, reducing performance.

The surface of GDE 3 appears to be covered with PA, except for a PTFE agglomeration in the image center (see Figure 2c). All pores of the CL seem to be flooded with PA. In contrast, the pore structure of GDE 4 (see Figure 2d) is still visible; although, not as clearly as in GDE 1 and 2. A PA layer covers the electrode structure, which reduces the image resolution. However, compared to GDE 3, the electrolyte layer seems thinner, and larger pores are not filled. While both GDEs were implemented into a full cell and heated to 160 °C for 120 h, only GDE 4 was operated under a constant current of 200 mA cm^{-2}. The water produced by the electrochemical reaction decreases the PA viscosity, leading to faster GDE percolation and improved PA distribution, which is beneficial for cell break-in.[26,30] EIS

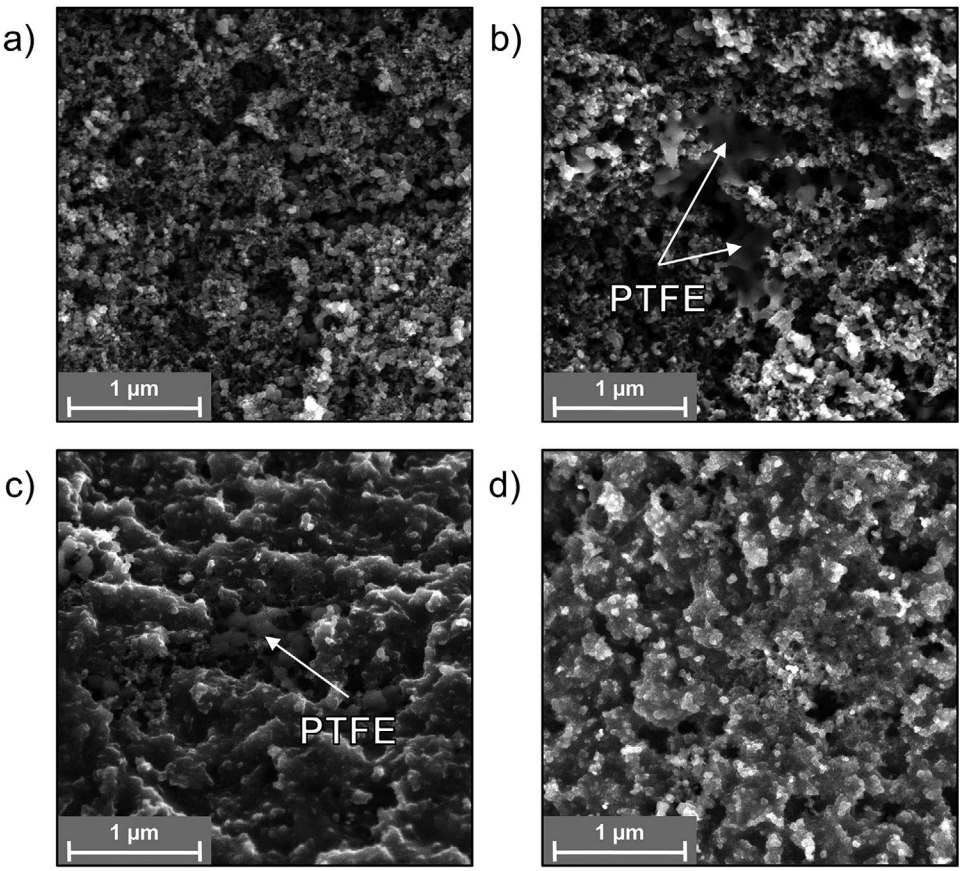

Figure 2. Top–down SEM images of the catalyst layer surface of a) GDE 1 recorded at 20 °C, b) GDE 2 recorded at –150 °C, c) GDE 3 after the operation (160 °C, 0 mA cm^{-2}, 5 days) recorded at –150 °C, and d) GDE 4 after the operation (160 °C, 200 mA cm^{-2}, 5 days) recorded at –150 °C.

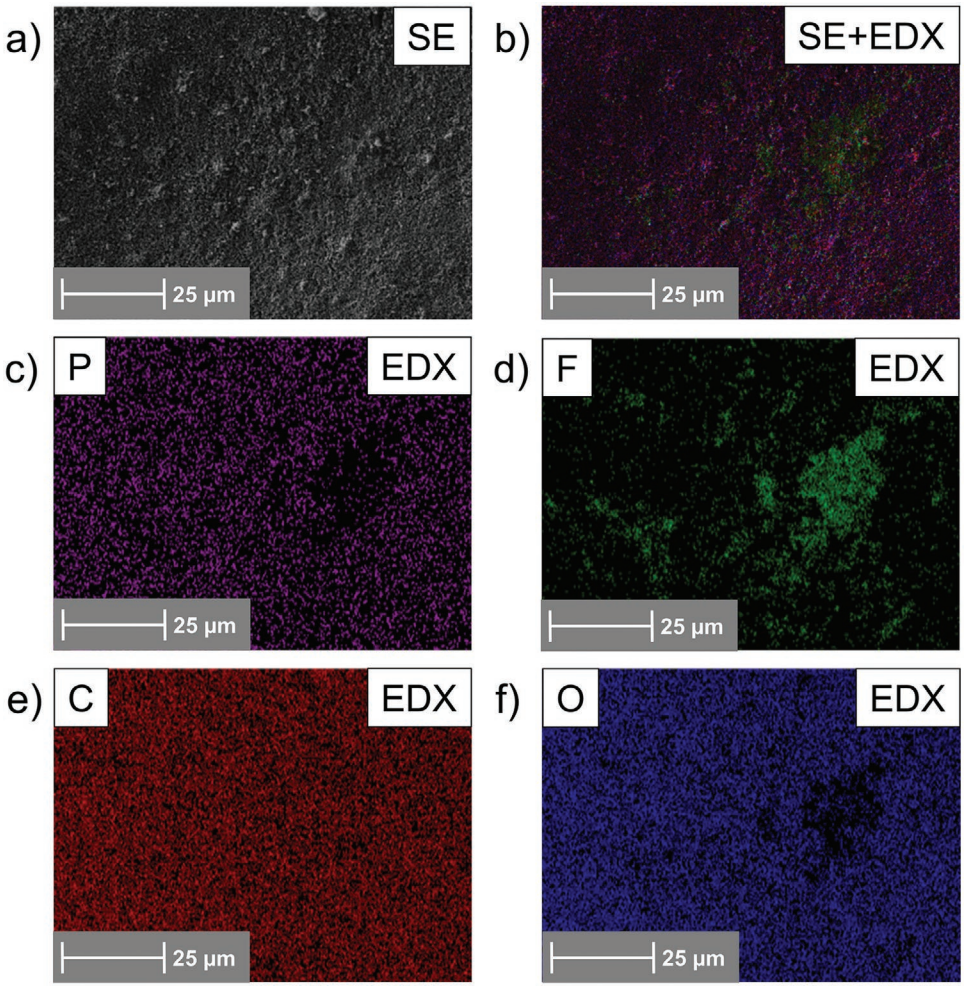

Figure 3. a) Top–down SE image of the CL surface of GDE 4 recorded at –150 °C after the operation and b) the corresponding mixed SE and EDX image showing the distribution of fluorine and phosphor, and the corresponding EDX maps of c) phosphor, d) fluorine, e) carbon, and f) oxygen.

with DRT analysis results of GDE 4 presented in Figure S1, Supporting Information show that the performance improvement during the break-in can be attributed to a decrease in the mass transport and the ORR impedance. The redistribution of PA inside the CL can free up bigger pores for gas transport; thus, reducing the mass transport resistance. Furthermore, the ORR is improved because the triple phase boundary is enlarged when more platinum catalyst gets covered by PA. These results suggest that the PA not only redistributes on a larger scale into the outer regions of the GDE but also reallocates in pores on the nanometer scale. Both effects combined to improve the cell performance during the break-in period.

Figure 3 presents EDX maps depicting the distributions of phosphor, fluorine, carbon, and oxygen on the surface of GDE 4. Carbon is the base material of the electrode and was therefore detected uniformly. The PA is represented by the phosphor and oxygen signals. The fluorine signal maps the PTFE binder. PTFE agglomerations of ≈1 to 10 µm are equally distributed over the CL surface, except for one large agglomeration with a diameter of 25 µm. A similar distribution and PTFE particle size were previously determined by EDX mapping in the cross-section of a catalyst layer with 10% PTFE.[11] Figure 3c,d shows that the PA is homogenously located on the CL surface, except at larger PTFE agglomerations. Thus, PTFE effectively repels PA in porous CL structures even at elevated temperatures. EDX maps of GDE 1 to 3 are shown in Figures S2–S4, Supporting Information.

The surface of each GDE was mapped at three sites to determine each element's mean weight percentage and standard deviation (see **Table 2**). A similar composition was measured for GDE 1 and 2, which validates that freezing in liquid nitrogen has no impact on the CL composition. The slight deviation in the fluorine content can be attributed to the formation of PTFE

Table 2. Catalyst layer surface composition of all GDEs determined by EDX.

Sample	Weight%				
	C	F	O	P	Pt
GDE 1	94.0 ± 1.4	4.7 ± 1.4	1.3 ± 0.2	–	–
GDE 2	92.0 ± 0.8	6.3 ± 1.1	1.7 ± 0.3	–	–
GDE 3	21.8 ± 2.0	5.3 ± 2.8	45.7 ± 1.3	27.2 ± 2.5	–
GDE 4	38.1 ± 0.9	6.8 ± 1.4	33.3 ± 1.2	14.4 ± 0.5	7.5 ± 1.1

agglomerations, which lead to uneven distributions.[9–11] For this reason, a more significant deviation is observed for the fluorine signal than for the other elements' signal.

On GDE 3, mainly phosphor and oxygen were detected. This result confirms the observation of the SE image in Figure 2c, where PA mainly covered the surface of GDE 3. Significantly less PA is detected on GDE 4, validating the SE image observation that less PA covers the surface. In GDE 4, platinum is also detected, which could potentially skew the other values. However, the signal intensity for P and O in the raw data (for spectra, see Figure S6, Supporting Information) is approximately a decade higher for GDE 3 than GDE 4, confirming more PA on GDE 3.

Contrary to these results, water production typically supports the PA movement into the electrodes, resulting in a higher PA content in GDE 4 compared to GDE 3. Possibly GDE 3 is not entirely percolated by PA, and most of the PA is found on the examined interface between the GDE and the membrane. This assumption is supported by observing several completely uncovered areas in the bulk of GDE 3 (see Figure S5, Supporting Information). Thus, the total PA content is still lower in the bulk of GDE 3. Furthermore, water production might stabilize the PA cluster in the membrane. PA is bound to PBI due to acid–base interaction. If PA forms polyphosphates under dry conditions, the electrolyte's acidity decreases. Thus, the interactions between PA and the PBI membrane weaken considerably. Without this bonding, the PA disconnects easier from the membrane, possibly supporting the PA movement from the membrane into the electrodes.

The surface fluorine content is similar for the PA-doped GDEs 3 and 4 and the undoped GDEs 1 and 2, while the detected carbon share is significantly lower in the PA-doped GDEs. Therefore, the PA mainly covers the CL carbon structure, while the PTFE binder remains uncovered and repels the PA.

The P to O ratio in GDE 3 and 4 is different, suggesting higher water content in GDE 4 caused by the water formation due to the operation under current density. In GDE 3, the P to O molar ratio of 1 to 3.3 is below that of orthophosphoric acid (1 to 4), indicating that the PA is partially present as polyphosphate. The operation under dry gas feed at high temperatures favors the dehydration of PA. GDE 4 exhibits a P to O molar ratio of 1 to 4.5. Assuming PA is entirely present in the form of H_3PO_4, the electrolyte consists of 8.2 wt% water. The increased water content of PA decreases the electrolyte viscosity, which supports its movement into the GDE.

3.2. Cathode Catalyst Layer Bulk Morphology and Composition

Figure 4 presents SE and BSE images recorded at the identical spot in the bulk of GDE 4. The SE images are blurry, which indicates that most of the electrode bulk is covered by PA. This

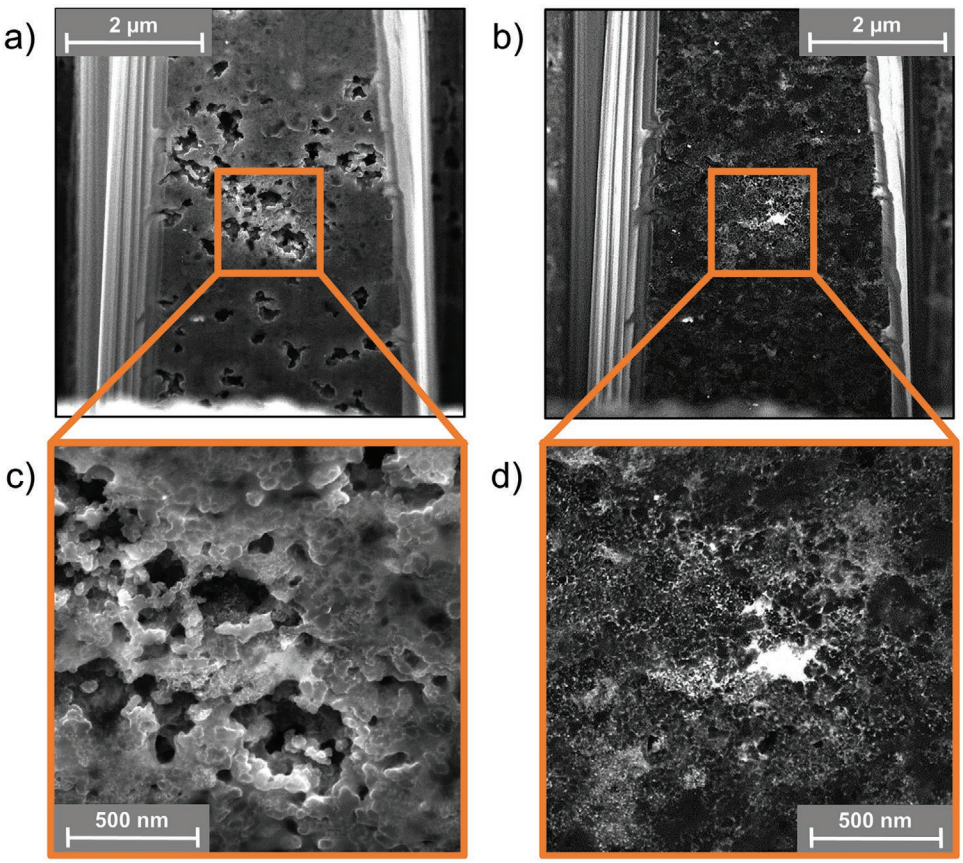

Figure 4. a) Top–down SE image and b) corresponding BSE image of the same section in the bulk of GDE 4, and c,d) magnification of the highlighted areas of (a,b).

observation confirms previous electron probe microanalysis (EPMA) experiments, which suggests a uniform PA distribution in the electrode, even after 12 000 h of operation.[31] However, no comparison to the binder distribution was drawn, and a different binder, polyvinylidene fluoride (PVDF), was utilized in this study. Furthermore, the PA distribution in the nanometer-sized pores could not be studied because the resolution of EPMA was limited to ≈1 µm.

Due to the high resolution of cryo FIB-SEM images, the PA distribution in pores below 1 µm can be investigated, which provides valuable insights into the preferred location of PA in the electrode pore structure. Larger pores in the CL with a diameter above ≈200 nm are not filled with PA (see Figure 4a,c). Previous NMR studies suggested that micropores are invaded before mesopores during the PA doping process because capillary forces draw PA into smaller pores.[32] The preferred PA invasion of the smaller pores was furthermore demonstrated by MEA testing over 3500 h with different MPLs. The MPL exhibiting a coarser carbon structure (graphitized carbon) reduced PA uptake and acid leaching significantly compared to a MPL with a fine pore structure (carbon black).[25] The presented SEM images indicate that all smaller pores are filled with PA, while some larger pores are void.

The bright spots in the BSE images (see Figure 4b,d) are ascribed to the platinum catalyst particles because platinum atoms are significantly heavier than the remaining elements in the CL. They are detected in the entire electrode bulk, even in areas indicated to be covered by PA in the corresponding SE image. Thus, the platinum signal must originate from below the PA layer. With Monte–Carlo simulations, the depth of the BSE signal was estimated to be ≈100 nm. The corresponding interaction volume of the BSE and X-ray signals is displayed in **Figure 5**. As no carbon structure is detected in most of the SE images, the PA layer has to be at least several nanometers thick as the SE signal originates from just below the surface. However, it is mostly thinner than 100 nm because platinum particles can still be detected below the electrolyte. Furthermore, no large, fully flooded, or arid area was found in GDE 4. These findings indicate that the PA forms a thin layer over the entire electrode at optimized phosphoric acid doping. However, bulk images of GDE 3 (see Figure S5, Supporting Information) display a more heterogeneous PA distribution, which further underlines the importance of water production during the break-in period and the influence of the cell potential in achieving a uniform PA distribution in the CL.

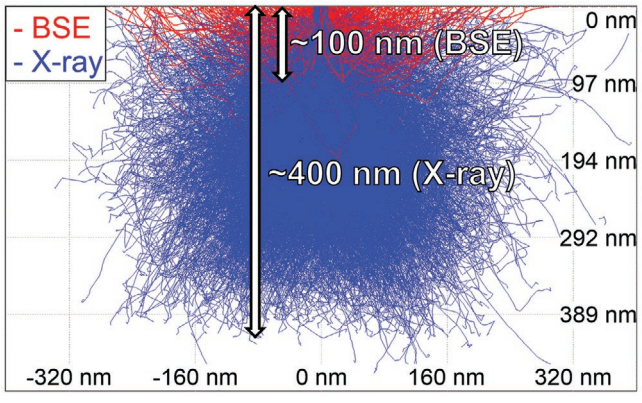

Figure 5. Interaction volume and estimated signal depth of the BSE and X-ray signals obtained by Monte-Carlo simulation performed with CASINO (v2.4.8.1).

ToF-SIMS measurements were performed complementary to SEM and EDX imaging. The ejected fragment with the highest signal intensity was chosen to depict the carbon (C_2) and the PA (PO_2) in the following images. **Figure 6** presents the ToF-SIMS maps of different atoms and molecules of GDE 4 seen from the electrode surface, which corresponds to the interface of the CL and the membrane in the assembled cell. Note that the signal intensity represented by the color scale is different for each signal. The signal intensity does not correspond to the atomic share of each element in the sample because the ionization probability of every molecule is different. However, each element can be located and related to the electrode structure, represented by the carbon signal. As the resolution of FIB-SEM coupled with ToF-SIMS is ≈100 nm with the recording parameters of this work, no information about the PA distribution in pores in the lower nanometer range could be obtained.

The carbon signal is relatively homogenous in the investigated area, except for three larger cracks with a width of ≈1 µm. The formation of shrinkage cracks in the CL occurs during the evaporation of the catalyst ink solvent and is a result of the fabrication process.[33] The fluorine signal shows several spherical PTFE agglomerations, mostly with a diameter between 5 and 10 µm. The mainly spherical shape of PTFE binder in HT-PEM FC electrodes was previously demonstrated by atomic force microscopy (AFM) experiments.[33] However, these results suggest a PTFE particle size of only 100 nm. The discrepancy in particle size suggests that the spherical PTFE particles of the commercial PTFE suspension agglomerate to larger particles during the ink preparation process and the spraying of the CL. While the AFM resolution is sensitive enough to detect individual segments agglomerated, the lower resolution of ToF-SIMS only allows monitoring the entire agglomeration.

The ToF-SIMS signals of oxygen and PO_2 represent phosphoric acid, which is uniformly distributed in the electrode. The PA and fluorine signals display contradictory trends: Areas with a high PO_2 signal show low fluorine content and vice versa, which confirms that PTFE effectively repels PA. Furthermore, the PA and the carbon signals are in excellent agreement, confirming that the PA is mainly located on the surface of the carbon structure. In the cracks of the electrode, no PA was detected. These findings coincide with the SEM images of the electrode bulk, which showed no PA in larger pores (see Figure 4).

Synchrotron studies by Halter et al. and Eberhardt et al. suggest that small cracks below 20 µm are less prone to flooding than medium-sized or larger cracks below 60 µm in width. The latter facilitates acid movement into the electrodes and serves as a pathway for PA.[14,16] These large cracks are undesirable because they increase acid leaching and accelerate degradation, especially if they penetrate the entire CL.[14] While X-ray imaging is suitable for studying the PA movement and loss in situ on a larger scale, its resolution makes it impossible to observe PA in pores below 1 µm. NMR studied the interaction of phosphoric acid with micropores and mesopores in carbon.[19] However, these experiments were performed ex situ,

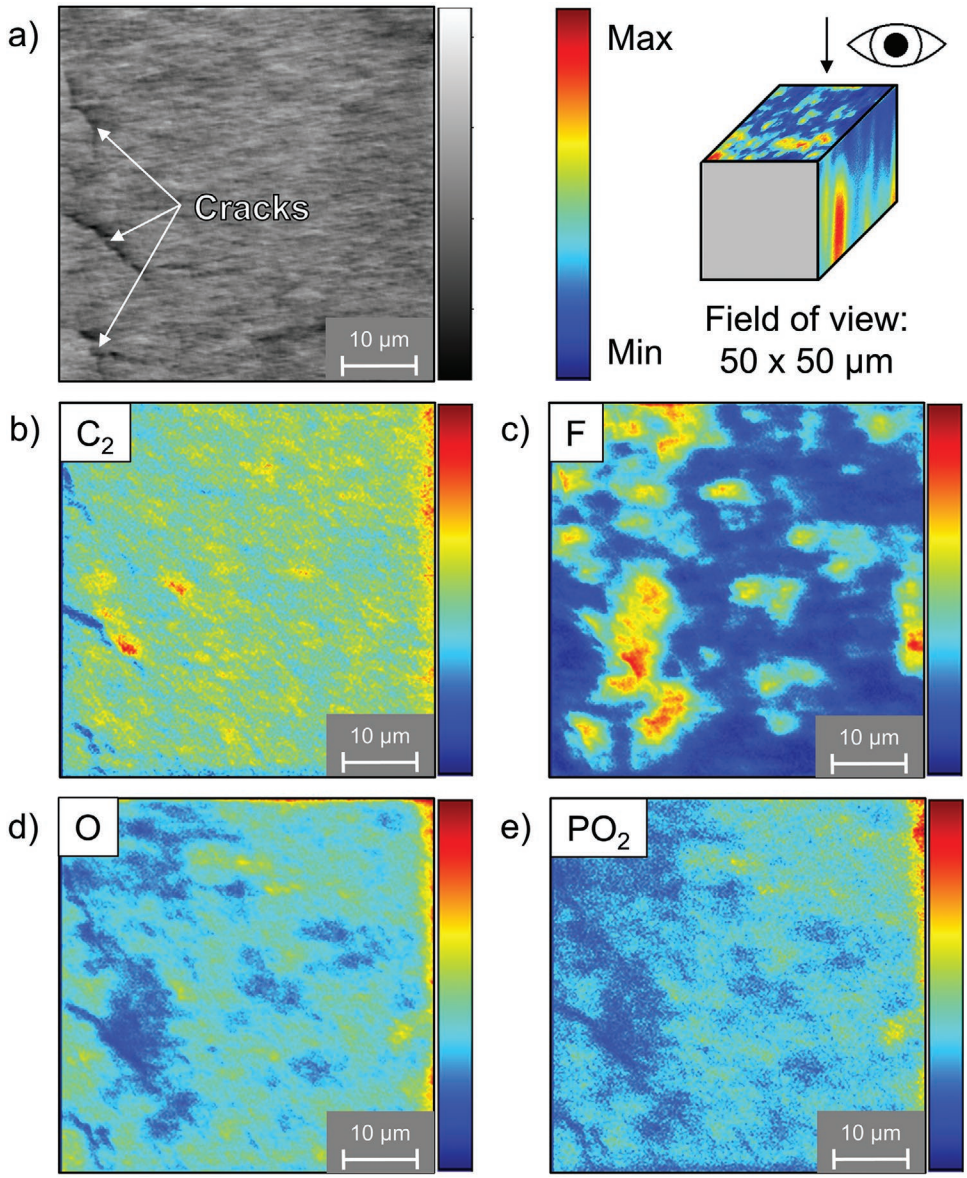

Figure 6. a) Top–down SE image of GDE 4 after operation recorded before sputtering and corresponding ToF-SIMS maps of b) carbon, c) fluorine, d) oxygen, and e) PO_2.

so the influence of the applied potential and water produced by the electrochemical reaction cannot be investigated. FIB-SEM coupled with ToF-SIMS is an excellent method to study PA in GDEs in the resolution gap between X-ray imaging (>1 µm) and NMR (<mesopores, 50 nm). While no in situ studies of FCs can be undertaken, examining operated cells with frozen PA distribution permits quasi in situ investigation.

Studies on the PA injection by µ-computed tomography (resolution: 1.86 µm) and by synchrotron combined with pore network modeling (PNM) confirm that large cracks in the MPL increase PA leaching.[32,34] However, if a crack-free MPL was employed, a pressure build-up was observed in the CL, and PA leaching was significantly reduced. Subsequently, increased capillary fingering leads to increased PA saturation in the electrode over the entire pore size range. In our study, the same crack-free MPL as in ref. [32] was employed, which confirms these PNM simulation results with higher resolution because PA wets the entire CL. Strong interaction between the hydrophilic carbon black and the PA favors covering the CL structure before filling the void in cracks and larger pores. As the CL in this study did not exhibit cracks above 1 µm in width, the PA behavior could not be studied in larger cracks, and no comparison to the results of Halter et al. could be drawn. While the MPL and CL in this study are nearly crack-free, the GDE employed by Halter et al. exhibited crack widths up to 150 µm, which significantly impacted the PA migration behavior and the capillary pressure.[35]

The bulk distributions of carbon, fluorine, oxygen, and PO_2 of GDE 4 mapped by ToF-SIMS are presented in **Figure 7**. The images in Figure 7 were recorded at the same spot as those in

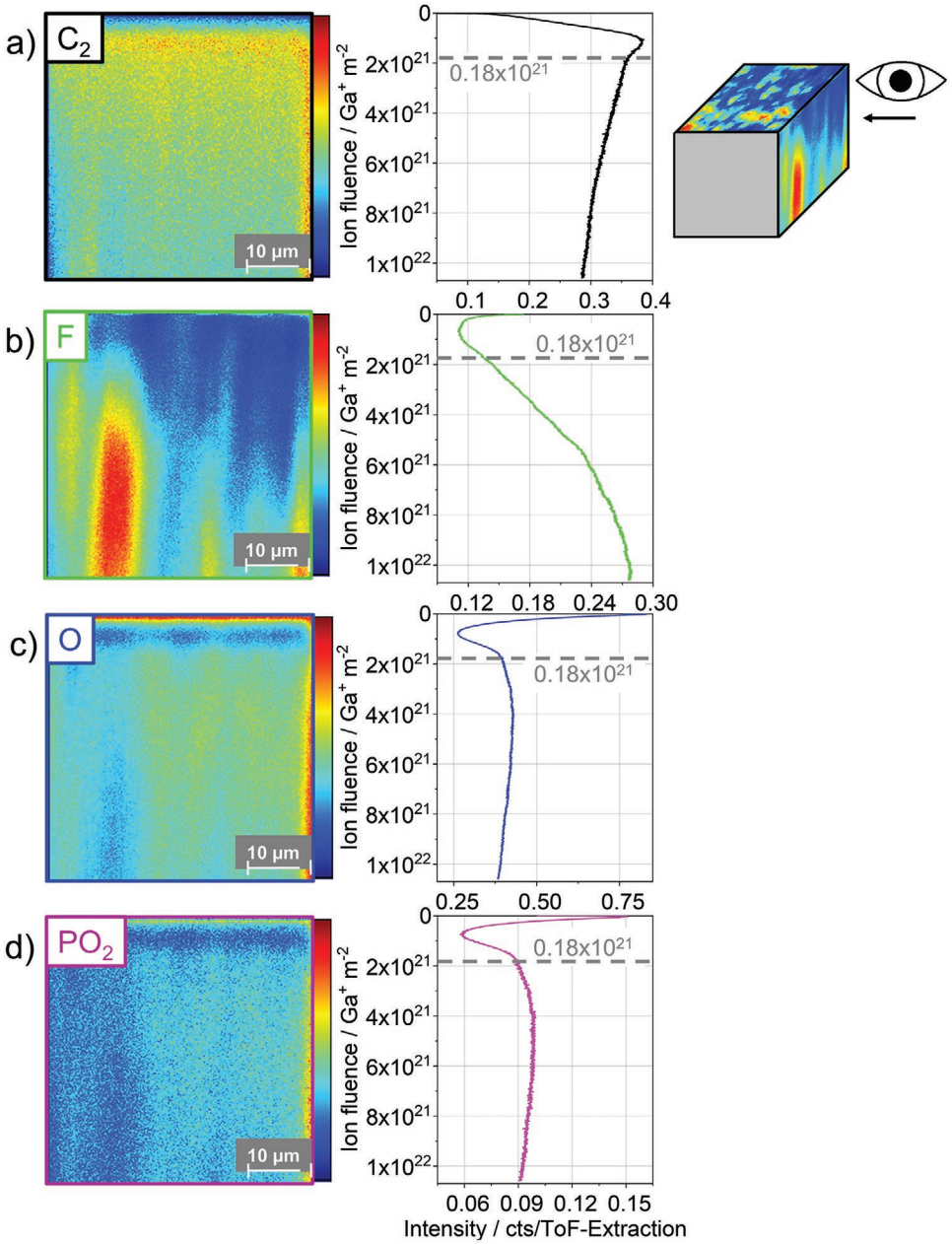

Figure 7. Cross-section distribution of a) carbon, b) fluorine, c) oxygen, and d) PO_2 of GDE 4 after cell operation and corresponding depth profile of each element determined by ToF-SIMS.

Figure 6. The element distributions in the cross-section of the CL were mapped a few nanometers below the electrode surface. The sputtering was performed starting on the interface of the CL and the membrane. With increasing ion fluence, deeper layers of the electrode were investigated. Carbon is found in the entire bulk, and the PA is homogeneously distributed, except at the PTFE agglomerations. Concentration profiles across the bulk were extracted for each fragment from these images. Significant changes in the CL composition were detected until 0.18×10^{21} Ga^+ m^{-2}, probably due to surface structure inhomogeneity caused during the separation of the cathode GDE from the MEA. Below 0.18×10^{21} Ga^+ m^{-2}, the PTFE content increases continuously. However, ToF-SIMS measurements performed on GDE 1 to 3 and at different sites of GDE 4 found no trend regarding the bulk distribution of the binder. Instead, it seemed to be randomly distributed in the CL. The increasing PTFE content slightly decreased the carbon and PA signals at higher ion fluence. However, the PTFE content seemed to be increasing substantially, while the PA content was nearly unaffected. Fluorine has a high ionization probability due to its high electron affinity; and therefore, a higher signal intensity at an identical share in the sample. Thus, the ToF-SIMS signals are distorted toward PTFE. Hence, quantitatively comparing the different materials and their gradients over the ion fluence was

inadequate. Nonetheless, the opposite slope of PTFE and PA signals could be qualitatively observed.

4. Conclusion

Distributions of phosphoric acid, PTFE binder, and carbon support were mapped by cryogenic FIB-SEM coupled with EDX and ToF-SIMS throughout a HT-PEM FC cathode catalyst layer. EDX mapping revealed PA covering the entire surface of the electrode, except for PTFE agglomerations. The SE images of the GDE surface and bulk displayed that phosphoric acid was present throughout the electrode, except for larger pores with a diameter above ≈200 nm. In addition, BSE images indicated that a PA layer covers platinum catalyst nanoparticles. With a Monte-Carlo simulation, the originating depth of the BSE signal was estimated to be 100 nm, which suggests that the PA forms a thin layer over the CL structure with a thickness below 100 nm.

In addition, a 3D distribution of all electrode components with a resolution of 100 nm was obtained with ToF-SIMS. PA was located throughout the examined GDE volume, except at larger cracks with widths above 1 µm and PTFE agglomerations. No dry zones were found in the cathode after the break-in period, which suggests complete wetting of the CL with PA. The high-resolution mapping of the PA distribution in HT PEM FCs by cryo ToF SIMS provides new insights into the electrolyte distribution in catalyst layers. This technique could be applied to study the interaction between PA and novel binder and catalyst materials, which will be beneficial for designing GDEs with improved cell performance.

Supporting Information

Supporting Information is available from the Wiley Online Library or from the author.

Acknowledgements

This work contributes to the research performed at CELEST (Center for Electrochemical Energy Storage Ulm-Karlsruhe).

Open access funding enabled and organized by Projekt DEAL.

Conflict of Interest

The authors declare no conflict of interest.

Data Availability Statement

The data that support the findings of this study are available from the corresponding author upon reasonable request.

Keywords

focused ion beam scanning electron microscopy (FIB-SEM), high-temperature polymer electrolyte membrane fuel cells (HT-PEM FC), phosphoric acid distribution, polybenzimidazole (PBI), time-of-flight secondary ion mass spectrometry (ToF-SIMS)

Received: December 4, 2022
Revised: February 17, 2023
Published online:

[1] Q. He, X. Yang, W. Chen, S. Mukerjee, B. Koel, S. Chen, *Phys. Chem. Chem. Phys.* **2010**, *12*, 12544.
[2] R. Zeis, *Beilstein J. Nanotechnol.* **2015**, *6*, 68.
[3] J. O. Park, K. Kwon, M. D. Cho, S.-G. Hong, T. Y. Kim, D. Y. Yoo, *J. Electrochem. Soc.* **2011**, *158*, B675.
[4] D. Ergun, Y. Devrim, N. Bac, I. Eroglu, *J. Appl. Polym. Sci.* **2012**, *124*, E267.
[5] K. S. Lee, J. S. Spendelow, Y. K. Choe, C. Fujimoto, Y. S. Kim, *Nat. Energy* **2016**, *1*, 16120.
[6] V. Atanasov, A. S. Lee, E. J. Park, S. Maurya, E. D. Baca, C. Fujimoto, M. Hibbs, I. Matanovic, J. Kerres, Y. S. Kim, *Nat. Mater.* **2021**, *20*, 370.
[7] C. Wannek, I. Konradi, J. Mergel, W. Lehnert, *Int. J. Hydrogen Energy* **2009**, *34*, 9479.
[8] P. Mazúr, J. Soukup, M. Paidar, K. Bouzek, *J. Appl. Electrochem.* **2011**, *41*, 1013.
[9] F. Mack, T. Morawietz, R. Hiesgen, D. Kramer, R. Zeis, *ECS Trans.* **2013**, *58*, 881.
[10] F. Mack, T. Morawietz, R. Hiesgen, D. Kramer, V. Gogel, R. Zeis, *Int. J. Hydrogen Energy* **2016**, *41*, 7475.
[11] S. Liu, K. Wippermann, W. Lehnert, *Int. J. Hydrogen Energy* **2021**, *46*, 14687.
[12] J. Müller-Hülstede, T. Zierdt, H. Schmies, D. Schonvogel, Q. Meyer, C. Zhao, P. Wagner, M. Wark, *J. Power Sources* **2022**, *537*, 231529.
[13] S. H. Eberhardt, M. Toulec, F. Marone, M. Stampanoni, F. N. Büchi, T. J. Schmidt, *J. Electrochem. Soc.* **2015**, *162*, F310.
[14] J. Halter, N. Bevilacqua, R. Zeis, T. J. Schmidt, F. N. Büchi, *J. Electroanal. Chem.* **2020**, *859*, 113832.
[15] W. Maier, T. Arlt, K. Wippermann, C. Wannek, I. Manke, W. Lehnert, D. Stolten, *J. Electrochem. Soc.* **2012**, *159*, F398.
[16] S. H. Eberhardt, F. Marone, M. Stampanoni, F. N. Büchi, T. J. Schmidt, *J. Electrochem. Soc.* **2016**, *163*, F842.
[17] I. J. Sanders, T. L. Peeten, *Carbon Black: Production, Properties and Uses*, Nova Science Publishers Inc., Hauppauge, NY **2011**.
[18] N. Bevilacqua, T. Asset, M. A. Schmid, H. Markötter, I. Manke, P. Atanassov, R. Zeis, *J. Power Sources Adv.* **2021**, *7*, 100042.
[19] E. Zhang, N. Fulik, H. Zhang, N. Bevilacqua, R. Zeis, F. Xu, E. Brunner, S. Kaskel, *Chem. Commun.* **2021**, *57*, 2547.
[20] M. Rohnke, K. Schaepe, A. K. Bachmann, M. Laenger, J. Janek, *Appl. Surf. Sci.* **2017**, *422*, 817.
[21] R. Kiebach, W. Zhang, M. Chen, K. Norrman, H. J. Wang, J. R. Bowen, R. Barfod, P. V. Hendriksen, W. Zhang, *J. Power Sources* **2015**, *283*, 151.
[22] R. Kanarbik, P. Möller, I. Kivi, E. Lust, *ECS Trans.* **2013**, *57*, 581.
[23] J. D. Fairweather, P. Cheung, D. T. Schwartz, *J. Power Sources* **2010**, *195*, 787.
[24] Y. Chung, C. Pak, G. S. Park, W. S. Jeon, J. R. Kim, Y. Lee, H. Chang, D. Seung, *J. Phys. Chem. C* **2008**, *112*, 313.
[25] A. Kannan, Q. Li, L. N. Cleemann, J. O. Jensen, *Fuel Cells* **2018**, *18*, 103.
[26] S. Galbiati, A. Baricci, A. Casalegno, G. Carcassola, R. Marchesi, *Int. J. Hydrogen Energy* **2012**, *37*, 14475.
[27] T. H. Wan, M. Saccoccio, C. Chen, F. Ciucci, *Electrochim. Acta* **2015**, *184*, 483.

[28] N. Bevilacqua, M. A. Schmid, R. Zeis, *J. Power Sources* **2020**, *471*, 228469.
[29] A. Weiß, S. Schindler, S. Galbiati, M. A. Danzer, R. Zeis, *Electrochim. Acta* **2017**, *230*, 391.
[30] W. Maier, T. Arlt, C. Wannek, I. Manke, H. Riesemeier, P. Krüger, J. Scholta, W. Lehnert, J. Banhart, D. Stolten, *Electrochem. Commun.* **2010**, *12*, 1436.
[31] Y. Oono, A. Sounai, M. Hori, *J. Power Sources* **2012**, *210*, 366.
[32] N. Bevilacqua, M. G. George, A. Bazylak, R. Zeis, *ECS Trans.* **2017**, *80*, 409.
[33] F. Mack, M. Klages, J. Scholta, L. Jörissen, T. Morawietz, R. Hiesgen, D. Kramer, R. Zeis, *J. Power Sources* **2014**, *255*, 431.
[34] S. Chevalier, M. Fazeli, F. Mack, S. Galbiati, I. Manke, A. Bazylak, R. Zeis, *Electrochim. Acta* **2016**, *212*, 187.
[35] J. Halter, T. Gloor, B. Amoroso, T. J. Schmidt, F. N. Büchi, *Phys. Chem. Chem. Phys.* **2019**, *21*, 13126.